metals

MDPI

Article

Microstructural Evaluation and Tensile Properties for GTAW Weldments of Stainless Steel 304 Seam Pipes

Eunhye Park [1,2] and Byounglok Jang [1,*]

[1] Department of Advanced Materials Processing and Engineering, INHA Manufacturing Innovation School, Incheon 21999, Republic of Korea; eunhye301@hanmail.net
[2] Department of Special Welding, Korea Polytechnics II, Incheon 22121, Republic of Korea
* Correspondence: jang.bl@inha.ac.kr

Abstract

This study examines the microstructural characteristics and tensile properties of autogenous orbital gas tungsten arc (GTA) circumferential butt welds produced on commercially rolled 304 stainless steel seam pipes (outer diameter 38.1 mm, wall thickness 2.0 mm) for high-purity fluid distribution systems. A three-segment current profile was employed using an AMI 8-4000 orbital system, with peak currents of 70, 67, and 65 A for the penetration, remelting, and downslope (crater-fill) segments, respectively, under high-purity Ar (99.999%) shielding with back purging. Electron backscatter diffraction (EBSD) analysis, including image quality (IQ), inverse pole figure (IPF), and kernel average misorientation (KAM) mapping, showed that the weld metal consists of epitaxially grown columnar austenite grains strongly oriented along the solidification direction, whereas the heat-affected zone (HAZ) exhibits finer equiaxed grains with an increased Σ3 twin boundary fraction and elevated low-angle boundary fraction, indicative of partial recrystallization. Only sparse, discontinuous δ-ferrite stringers were detected in the fusion zone, and no non-metallic inclusions were observed on fracture surfaces, supporting the weld metal's suitability for semiconductor-grade cleanliness. Vickers microhardness profiles revealed modest hardness differences (typically within 10–20 HV) between the weld metal, HAZ, and base metal, with no pronounced HAZ softening. Cross-weld tensile tests conducted in accordance with ASTM E8/E8M-22 yielded yield strengths above 200 MPa, ultimate tensile strengths of 650–680 MPa, and total elongations approaching 40%, comparable to the as-received pipe. Scanning electron fractography confirmed fully ductile failure via microvoid coalescence without evidence of cleavage, intergranular decohesion, or weld-defect-induced embrittlement. Collectively, these results demonstrate that the three-segment autogenous orbital GTAW procedure produces structurally sound, particle-clean joints suitable for 304 stainless steel seam pipes used in high-purity industrial piping.

Keywords: stainless steel 304; GTAW; microstructure; heat effected zone; EBSD; tensile test

Academic Editor: Jiankang Huang

Received: 16 April 2026
Revised: 18 May 2026
Accepted: 18 May 2026
Published: 22 May 2026

1. Introduction

Austenitic stainless steel 304 is widely used for process-gas, vacuum, and fluid distribution piping in semiconductor manufacturing, pharmaceutical production, and general chemical processing facilities, owing to its good corrosion resistance, weldability, and cleanliness [1,2]. In many of these applications, pipes are fabricated from a rolled strip on continuous forming and welding lines, producing longitudinally welded seam pipes whose integrity is critical because local microstructural heterogeneities and weld-induced

defects can act as preferential sites for crack initiation, leakage, and particle generation under service conditions [3,4]. In addition to mechanical loading, welded stainless steel components may be exposed to erosive or corrosive environments; for example, Mousavi et al. showed that the erosion resistance of austenitic stainless steel is strongly influenced by surface hardness and microstructural condition, underscoring the importance of controlling weld metal and heat-affected zone (HAZ) properties [5].

Orbital gas tungsten arc welding (GTAW) has become the standard method for circumferential butt joints in stainless steel piping, particularly in high-purity industries, because the programmable control of the arc current, travel speed, and shielding gas allows for a highly reproducible bead geometry and a narrow HAZ with minimal operator dependence [1,6–8]. These advantages are especially important for thin-walled pipes, where excessive heat input readily causes burn-through, distortion, and loss of dimensional tolerance [9,10]. To meet demanding requirements for leak-tightness and cleanliness, orbital GTAW procedures often employ multi-segment or multi-layer current profiles that combine penetration, remelting, and downslope (crater-fill) stages; however, the microstructural consequences of such segmented procedures in commercially produced seam pipes have not been systematically quantified.

Numerous studies have investigated the microstructure and mechanical properties of GTAW-welded austenitic stainless steels. Widyianto et al. [2] reported that positional variations in heat input significantly influence bead geometry and grain morphology in orbital GTAW of 304L pipes. Riffel et al. [11,12] demonstrated that current waveform selection governs the solidification structure and δ-ferrite distribution in 304L/316L orbital welds, while Pham et al. optimized orbital TIG parameters for SUS 304 piping. Fadaei and Poursina examined the effect of thermal aging on the fracture toughness of GTAW/SMAW 316L joints and showed that prolonged exposure can modify δ-ferrite morphology and degrade impact resistance [13]. Park et al. highlighted the sensitivity of root penetration to joint fit-up in butt-welded thin sections, which is directly relevant to the orbital welding of small-diameter pipes [14]. Chen et al. achieved grain refinement via ultrasonic–magnetic-field hybrid GTAW of 304 stainless steel, illustrating that process modifications can significantly alter weld microstructures [15].

Despite this substantial body of work, most investigations have focused on solution-annealed plates, thick-walled pipes, or dissimilar joints, and systematic data for commercially produced 304 seam pipes—with rolled austenitic microstructures and residual deformation substructures from forming—remain limited [10,16,17]. When a circumferential orbital GTAW weld is superimposed on such a thermomechanically processed substrate, the resulting microstructures and textures can differ markedly from those in solution-annealed plate welds, and multi-segment remelting strategies introduce additional thermal cycles that govern solidification texture, δ-ferrite morphology, grain boundary character distribution, and residual strain [18–20]. Furthermore, while previous studies have separately characterized EBSD features, hardness profiles, or tensile properties, there is a lack of integrated, quantitative correlations between EBSD-derived crystallographic parameters (grain size, HAGB/LAGB fractions, Σ3 twin boundaries, KAM distributions) and mechanical performance for autogenous orbital GTAW of thin-walled 304 seam pipes.

The present study addresses these gaps by investigating the microstructural evolution and tensile properties of autogenous orbital GTA circumferential butt welds produced on commercially available 304 stainless steel seam pipes (outer diameter 38.1 mm, wall thickness 2.0 mm) using a three-segment current profile. The weld metal, HAZ, and base metal are characterized by optical microscopy and electron backscatter diffraction (EBSD), including image quality (IQ), inverse pole figure (IPF), grain boundary (GB) character, and kernel average misorientation (KAM) mapping, together with quantitative grain size and

Σ3 boundary analysis. Vickers microhardness profiles are used to map strength variations across the longitudinal seam weld and two circumferential orbital welds. Cross-weld tensile tests in accordance with ASTM E8/E8M-22 [21] and SEM fractography are employed to establish quantitative microstructure–property relationships, with particular attention being paid to the ductility and fracture mode. By integrating these techniques, this work provides a microstructurally informed and quantitatively supported basis for qualifying and optimizing three-segment autogenous orbital GTAW procedures for 304 commercial seam pipes used in high-purity industrial piping systems.

2. Materials and Methods

2.1. Base Material and Pipe Geometry

The base material was a commercially produced longitudinally welded 304 austenitic stainless steel seam pipe with an outer diameter of 38.1 mm and a wall thickness of 2.0 mm, intended for high-purity fluid distribution applications. The pipe was manufactured from a cold-rolled strip on a continuous forming and welding line, producing a longitudinal seam weld followed by straightening and sizing. The as-received microstructure consisted of rolled γ-austenite with elongated grains and δ-ferrite stringers aligned along the pipe axis. The chemical composition supplied by the manufacturer satisfied the requirements of ASTM A312 for TP304 stainless steel [22], and no additional heat treatment was applied prior to circumferential orbital welding.

2.2. Orbital GTAW Procedure

Circumferential butt welds were produced using an AMI 8-4000 orbital gas tungsten arc welding (GTAW) system equipped with a closed welding head. Pipe ends were machined square and joined with a negligible root gap, representative of semiconductor-grade piping practice. High-purity argon (99.999%) was employed as both shielding and back-purge gas; the internal purge was maintained until the weld region cooled below approximately 150 °C in order to prevent oxidation of the inner surface.

An autogenous three-segment current profile was used to control penetration, remelting, and weld termination, as summarized in Table 1. The first segment (penetration segment) employed a peak current of 70 A and a rotation time of about 30 s to establish full-thickness penetration without burn-through. The second segment (remelting segment) used a peak current of 67 A with a rotation time of approximately 60 s, partially remelting the first-segment fusion zone to homogenize the weld metal and eliminate incipient defects. The third segment corresponded to a short downslope (crater-fill) stage with a peak current of 65 A and a duration of 1.7 s, during which the current was gradually reduced to fill the end crater and minimize termination-related cracking.

Table 1. Orbital GTAW parameters of butt GTAW stainless steel 304 seam pipes.

Segment	Peak Current (A)	Average Current (A)	Background Current (A)	Welding Time (s)
1 (0–360°)	70	45	20	30.0
2 (–720°)	67	41	15	60.8
3 (–730°)	65	40	15	1.7

The nominal heat input for each segment was estimated from

$$Q = \eta VI/v,$$

where η = 0.7 is the arc efficiency, V ≈ 12 V is the arc voltage, I is the average current, and v is the travel speed derived from the pipe circumference and rotation time. The calculated heat inputs were in the order of 0.10 kJ/mm for the penetration segment and approximately 0.09 kJ/mm for the remelting and downslope segments. Arc length, torch position, and shielding conditions were kept constant for all welds.

2.3. Microstructural Characterization

Transverse cross-sections of the longitudinal seam weld and of two circumferential orbital welds (designated Weld 1 and Weld 2) were cut using a low-speed diamond saw. Specimens were mounted in conductive phenolic resin, ground with SiC papers up to 2000 grit, and polished using 3 µm and 1 µm diamond suspensions, followed by a final polish with 0.04 µm colloidal silica.

Macro- and low-magnification images of the weld cross-sections were obtained using a digital microscope (VHX-7000, Keyence Corp., Osaka, Japan) to document the overall fusion zone, heat-affected zone (HAZ), and base metal (BM). For optical microscopy, selected cross-sections were etched with aqua regia to reveal the weld metal (WM), HAZ, and BM microstructures, including δ-ferrite stringers inherited from pipe forming.

Electron backscatter diffraction (EBSD) measurements were performed on the polished, unetched cross-sections using a field-emission scanning electron microscope, FE-SEM (SU8700, Hitachi High-Tech, Tokyo, Japan), equipped with a Velocity Super EBSD camera (EDAX, Mahwah, NJ, USA). EBSD data were acquired at an accelerating voltage of 20 kV, a probe current of approximately 5–7 nA, and a working distance of ~15 mm. For the longitudinal seam weld (Figure 1), a step size of 2.7 µm was used, corresponding to a minimum reliably measurable grain size of about 4.0 µm. For the circumferential orbital welds (Figure 2), a step size of 4.0 µm was used, giving a minimum grain size resolution of roughly 6.0 µm. These values were selected to provide at least ~10 measurement points across typical grains while maintaining practical scan times over the WM–HAZ–BM regions.

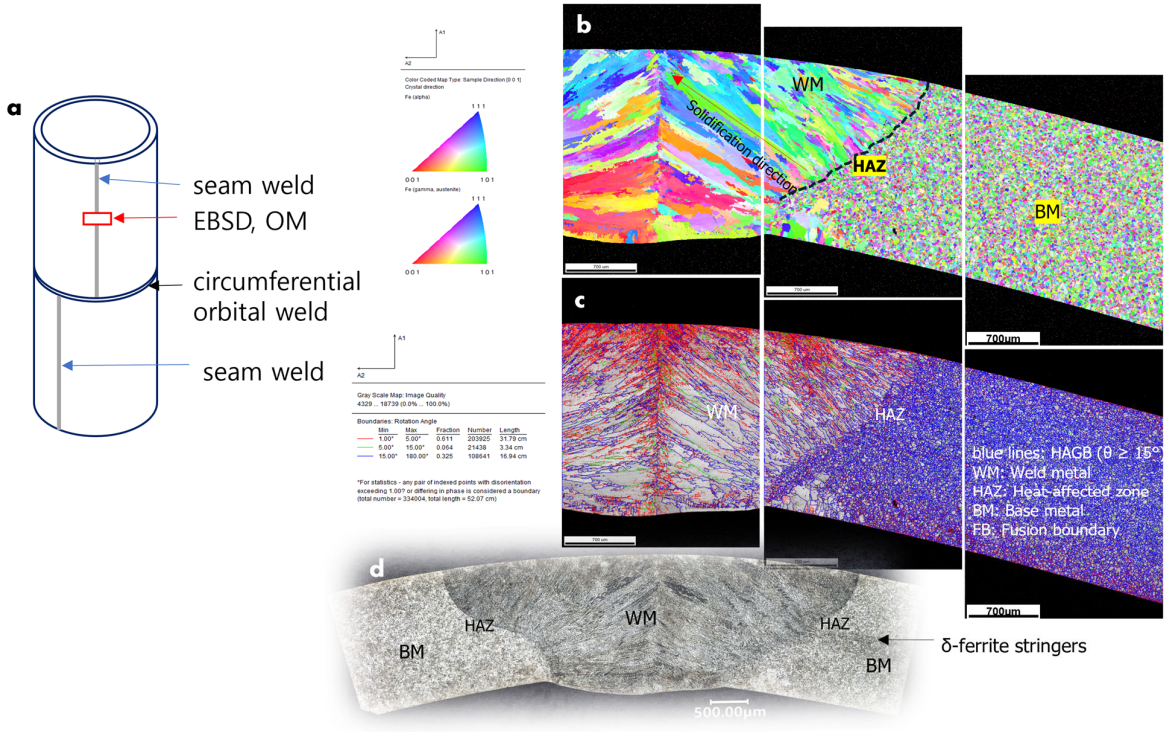

Figure 1. Geometry and microstructural characterization of the longitudinal seam weld in the 304 stainless steel seam pipe. (**a**) Schematic illustration of the pipe geometry showing the longitudinal

seam weld (along the pipe axis) and the location of the circumferential orbital GTAW weld, together with the cross-section cut used for EBSD and optical microscopy (WM–HAZ–BM). (**b**) Inverse pole figure (IPF) map of the FCC austenite phase (γ, projection//ND) across the seam weld, heat-affected zone (HAZ), and base metal (BM). (**c**) Grain boundary character map superimposed on the IQ map, where black lines denote random high-angle grain boundaries (HAGB, $\theta \geq 15°$) and red lines denote Σ3 twin boundaries; fusion boundaries (FB) are indicated by dashed lines. (**d**) Optical micrograph of the longitudinal cross-section confirming a sound fusion zone, a narrow HAZ, and the rolled austenitic microstructure with δ-ferrite stringers in the BM.

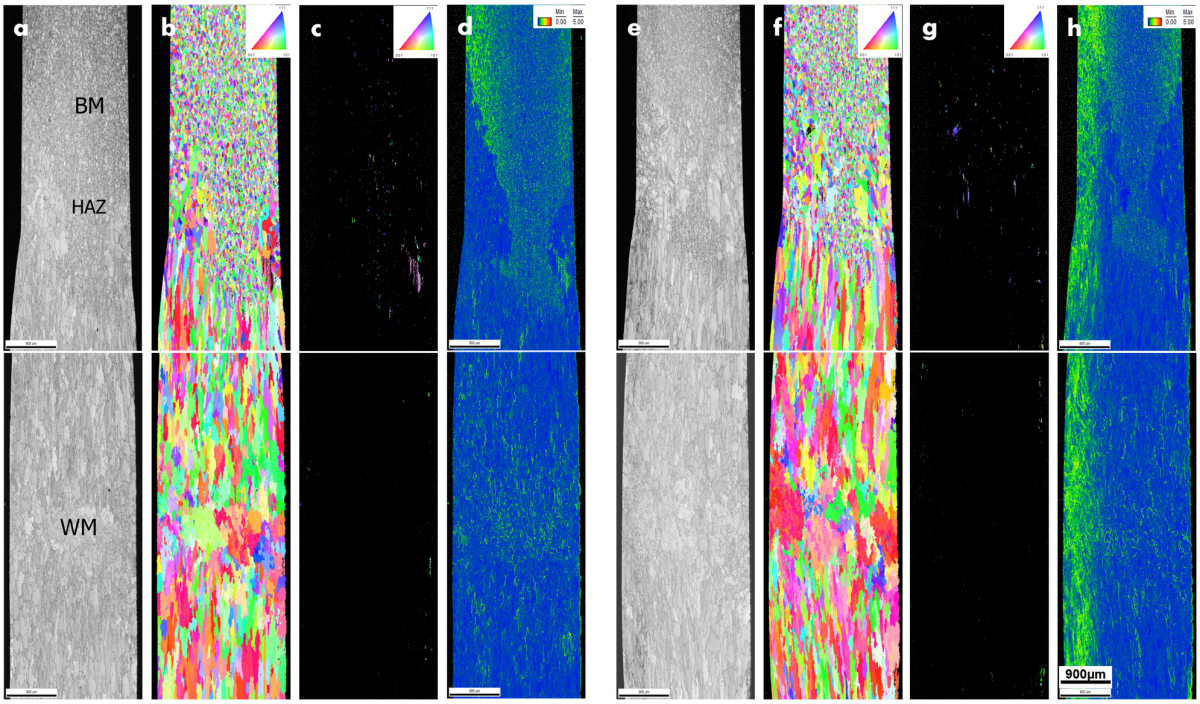

Figure 2. EBSD characterization of the two circumferential orbital GTAW welds on the 304 stainless steel seam pipe. (**a**–**d**) Weld 1 and (**e**–**h**) Weld 2. (**a**,**e**) Image quality (IQ) maps of the longitudinal cross-sections, indicating the base metal (BM), heat-affected zone (HAZ), and weld metal (WM). (**b**,**f**) Inverse pole figure (IPF) maps of the FCC austenite phase (γ, projection//ND) showing the transition from equiaxed grains in the BM and HAZ to columnar grains in the WM; the standard IPF color triangle (001–101–111) is shown in the upper-right corner. (**c**,**g**) IPF maps of the BCC δ-ferrite phase (projection//ND) revealing sparse δ-ferrite stringers aligned with the solidification direction. (**d**,**h**) Kernel average misorientation (KAM) maps calculated with a nearest-neighbor kernel and a maximum misorientation threshold of 5°, where higher KAM values indicate increased local lattice distortion and geometrically necessary dislocation density; the KAM color scale ranges from 0° (blue) to 5° (yellow). Fusion boundaries (FB) between WM and HAZ are marked by white dashed lines. Scale bars: 900 µm (all maps).

Raw EBSD data were cleaned by means of confidence index (CI) standardization and neighbor CI correlation, using a minimum grain size of 10 pixels and a grain tolerance angle of 5°. Image quality (IQ) maps, inverse pole figure (IPF) maps of the FCC austenite (γ) and BCC δ-ferrite phases (projection parallel to the normal direction, IPF//ND), grain boundary (GB) character maps, and kernel average misorientation (KAM) maps were generated using OIM ver.8 Analysis software. Grain size was quantified using the equivalent circle diameter (ECD) of reconstructed grains, and average grain size with standard deviation was calculated for WM, HAZ, and BM, with at least 500 grains analyzed per region.

Grain boundaries were classified into low-angle grain boundaries (LAGB, $2° \leq \theta < 15°$) and high-angle grain boundaries (HAGB, $\theta \geq 15°$). Boundary-length fractions of LAGB and HAGB were obtained from the total measured boundary length. Coincident site lattice (CSL)

Σ3 twin boundaries were identified using the Brandon criterion ($\Delta\theta \leq 15^\circ/\sqrt{\Sigma} = 8.66^\circ$ for Σ3), and their length fraction was calculated relative to the total HAGB length. KAM values were computed using a first-nearest-neighbor kernel with a maximum misorientation threshold of 5°. A fixed color scale of 0–5° was applied to all KAM maps so that absolute differences in local lattice distortion and geometrically necessary dislocation density could be compared directly among the WM, HAZ, and BM.

2.4. Mechanical Testing

2.4.1. Vickers Microhardness Procedure

Vickers microhardness measurements were conducted on the transverse cross-sections of the longitudinal seam weld and both circumferential orbital welds using a Vickers microhardness tester (HMV-G, Shimadzu Corp., Kyoto, Japan). A load of 4.9 N (≈500 gf) and a dwell time of 10 s were applied for all indentations. For each weld, two hardness traverses were performed: one at a near-surface position approximately 0.2 mm from the outer surface and one at mid-thickness approximately 1.0 mm from the outer surface. Indentations were placed at intervals of about 400 μm across the BM–HAZ–WM–HAZ–BM sequence.

At each location, three indentations were made, and the reported hardness value is the average of these three measurements. This procedure yielded 45 averaged data points per traverse (15 in BM, 10 in HAZ, 10 in WM, 10 in HAZ, and 15 in BM), providing sufficient spatial resolution to detect any softening or hardening in the HAZ and weld metal relative to the base metal.

2.4.2. Tensile Testing

Cross-weld tensile specimens were machined from the circumferential orbital welds such that the weld line was located at the mid-length of the gauge section. Sub-size flat specimens with a thickness of 2 mm, a gauge width of 6 mm, and a gauge length of 25 mm were prepared in accordance with ASTM E8/E8M-22. The longitudinal axis of each specimen coincided with the pipe axis, and the circumferential weld was centered within the gauge length. Four cross-weld specimens (Specimens 1–4) were tested to evaluate the reproducibility of the orbital GTAW procedure.

Tensile tests were carried out at room temperature using a universal testing machine (AGS-X, 20 kN capacity, Shimadzu Corp., Kyoto, Japan) under displacement control at a crosshead speed of 5 mm/min. Engineering stress–strain curves were recorded for all specimens. The 0.2% offset yield strength, ultimate tensile strength, and total elongation were determined from these curves. Additional specimens extracted from the as-received seam pipe without circumferential welds were tested under identical conditions to obtain the base-metal tensile properties for comparison.

2.5. SEM Fractography and Inclusion Assessment

After tensile testing, the fracture surfaces of the cross-weld specimens were examined using a field-emission scanning electron microscope, FE-SEM (JSM-7100F, JEOL Ltd., Tokyo, Japan), to identify the fracture mode and potential crack-initiation sites. Fractographs were acquired at multiple positions through the wall thickness (outer surface, upper mid-thickness, mid-thickness transition zone, lower mid-thickness, and inner surface) on both opposing fracture surfaces, typically at magnifications of ~×1000. The morphology and size distribution of dimples were analyzed to assess the dominance of microvoid nucleation, growth, and coalescence. Particular attention was paid to the presence of cleavage facets, intergranular decohesion, weld-related defects (porosity, lack of fusion), and non-metallic inclusions. No non-metallic inclusions or inclusion-induced fracture

origins were observed on any of the examined fracture surfaces, which is an important consideration for semiconductor-grade piping where particle cleanliness is critical.

3. Results

3.1. Microstructure of the Longitudinal Seam Weld

The EBSD and optical micrographs for the longitudinal cross-section of the welded joint in the 304 stainless steel seam pipe are presented in Figure 1. The inverse pole figure (IPF) maps, calculated for the austenitic FCC phase with respect to the <111> sample direction, reveal a pronounced change in grain morphology and orientation distribution from the fusion boundary toward the pipe wall. In the weld metal, columnar grains nucleate at the fusion line and grow epitaxially toward the weld centerline, producing bands of nearly uniform color that indicate a strong preferred orientation aligned with the local thermal gradient. Toward the outer regions of the fusion zone and into the HAZ, the IPF maps show a transition to finer, more equiaxed grains with a broader spread of orientations, reflecting a gradual recovery toward a more randomized texture.

The grain boundary (GB) maps reveal that high-angle grain boundaries form a continuous network along the columnar grain interfaces in the weld metal. Moving away from the fusion boundary, an increased frequency of equiaxed grains and a higher fraction of Σ3 twin boundaries are observed, which interrupt the connectivity of random high-angle boundaries. This change is indicative of recovery and partial recrystallization in the HAZ, where locally stored deformation energy from prior forming operations is released during the welding thermal cycle. In the base metal, elongated grains and stable twin boundary networks reflect the thermomechanical processing history of the seam pipe.

The optical micrograph of the same cross-section is consistent with the EBSD results. The weld metal exhibits a cast-like solidification structure with clearly defined fusion boundaries and a weld width in the order of several hundred micrometers. Adjacent to the fusion boundary, the HAZ shows gradual grain refinement, while the base metal retains its original rolled austenitic matrix with moderately elongated grains and local bands of δ-ferrite.

3.2. EBSD Analysis of Orbital GTAW Welds

The EBSD results for the two circumferential orbital GTAW welds are presented as IQ, IPF-fcc, IPF-bcc, and KAM maps in Figure 2. The IQ maps show that both fusion zones exhibit relatively high and uniform IQ values, consistent with a well-solidified austenitic matrix, whereas local dark bands at the fusion boundaries and along grain boundaries indicate regions of increased lattice distortion. Toward the HAZ and base metal, a finer-scale mottled contrast is observed, characteristic of the rolled 304 microstructure containing deformation substructures. The IPF-fcc maps reveal that columnar grains nucleate epitaxially at the fusion line and grow toward the weld centerline in both welds, producing elongated color bands with strong preferred orientations aligned with the solidification direction. However, the relative intensity and continuity of these bands differ between the two welds, suggesting subtle variations in thermal gradient and solidification conditions. In the adjacent HAZ, a transition to smaller, more equiaxed grains with a broader color distribution is observed.

3.3. Vickers Microhardness

The Vickers microhardness profiles measured across the 304 stainless steel seam pipe are shown in Figure 3. In the seam-weld region, the base metal hardness on both sides remains within a narrow band, indicating a uniform work-hardened and annealed condition from the pipe-forming process. The weld metal hardness is 10–20 HV higher than

the adjacent base metal, attributable to solidification substructure, residual δ-ferrite, and locally elevated dislocation density. The hardness distribution is comparatively symmetric with only modest surface-to-mid-thickness gradients.

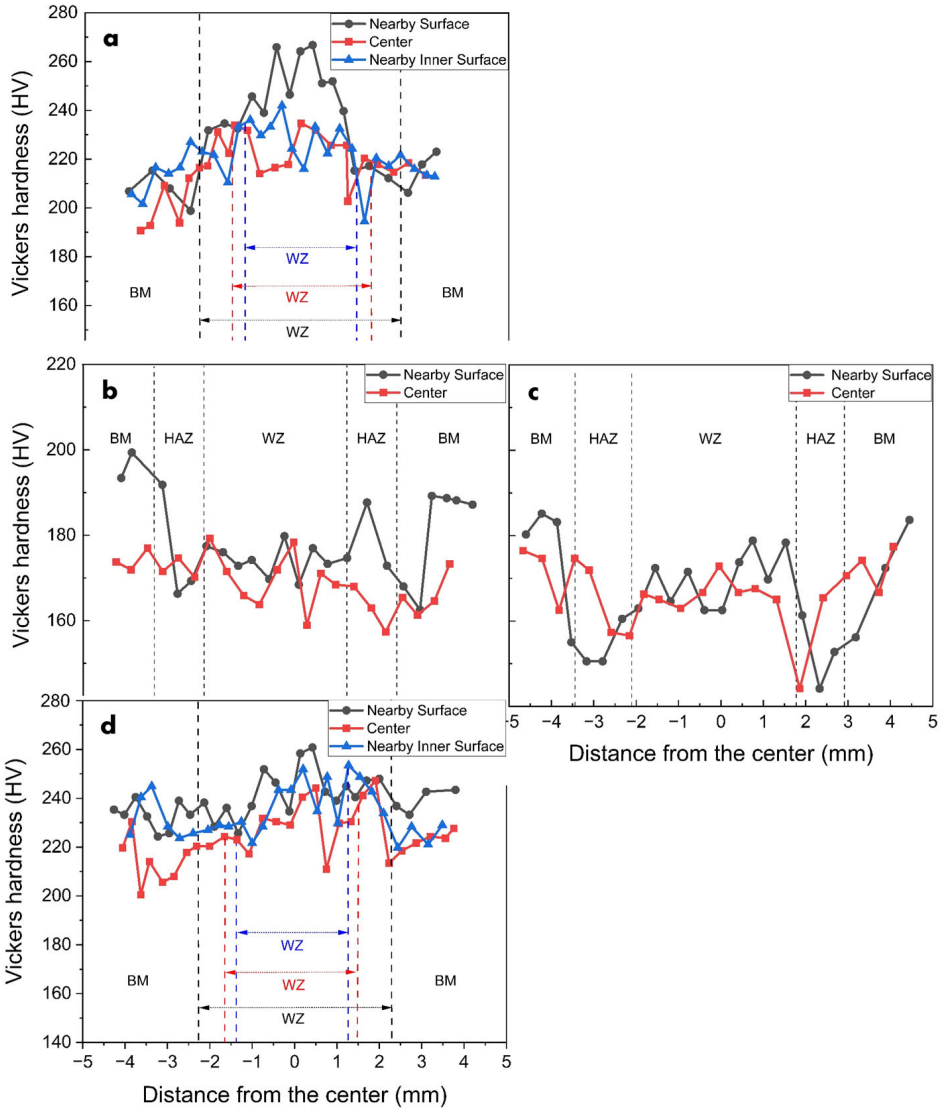

Figure 3. Vickers microhardness profiles measured across the transverse cross-sections of the 304 stainless steel seam pipe: (**a**) longitudinal seam weld on one side of the pipe; (**b**) circumferential orbital GTAW Weld 1 (two-pass region); (**c**) circumferential orbital GTAW Weld 2 (down-slope region); (**d**) longitudinal seam weld on the opposite side of the pipe. Filled symbols and open symbols represent measurements at near-surface (~0.2 mm from the outer surface) and mid-thickness (~1.0 mm from the outer surface) positions, respectively. The dashed vertical lines indicate the approximate fusion boundaries between the weld metal, heat-affected zone (HAZ), and base metal (BM). All hardness measurements were performed with a load of 200 gf, a dwell time of 10 s, and an indentation spacing of 250 μm.

For the two orbital GTAW welds, the base metal hardness far from the weld is similar to that of the seam region. Within the orbital weld metal, the average hardness is comparable to or slightly lower than that of the seam weld, and the profiles display noticeable differences between the near-surface and mid-thickness positions, indicating a stronger through-thickness thermal gradient typical of single-sided orbital GTAW. In one orbital weld, the weld metal hardness remains nearly flat, while in the other, a more pronounced

hardness maximum is observed near the weld center. The HAZs of both orbital welds show slight softening or fluctuating hardness relative to the base metal.

3.4. Tensile Properties

The engineering stress–strain curves of the four cross-weld specimens (Figure 4c) were highly reproducible, with only minor variation in both strength and ductility. The cross-weld specimens exhibited a 0.2% offset yield strength of 205 ± 8 MPa, an ultimate tensile strength of 665 ± 15 MPa, and a total elongation of 38 ± 2% (mean ± standard deviation, n = 4). For comparison, the as-received 304 stainless steel seam pipe showed a yield strength of 215 ± 5 MPa, an ultimate tensile strength of 680 ± 10 MPa, and an elongation of 42 ± 2% under the same testing conditions. Thus, the autogenous orbital GTAW joints retain approximately 95% of the base-metal strength and about 90% of the ductility, indicating that the three-segment orbital procedure does not significantly degrade the global mechanical performance of the pipe.

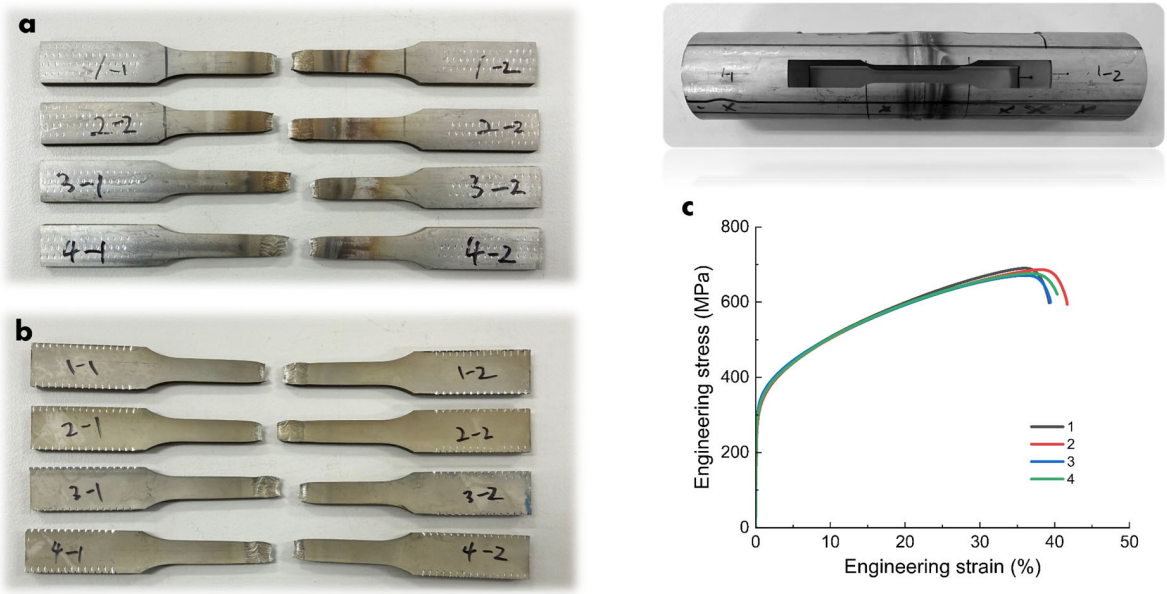

Figure 4. Cross-weld tensile testing of the circumferential orbital GTAW joints in the 304 stainless steel seam pipe. (**a**) Photographs of the four as-machined tensile specimens (Specimens 1–4), whose gauge sections contain the circumferential orbital GTAW weld at mid-length. (**b**) Corresponding specimens after tensile testing, showing uniform necking localized in the weld region with no evidence of brittle fracture or premature failure outside the weld. (**c**) Engineering stress–strain curves of the four cross-weld specimens tested in accordance with ASTM E8/E8M-22, demonstrating consistent yield and ultimate tensile strengths and large uniform elongations approaching ~40%.

3.5. Fracture Behavior

Post-test examination of the tensile specimens (Figures 5 and 6) shows that all four specimens develop well-defined necking localized within or immediately adjacent to the orbital GTAW weld region. The gauge sections exhibit smooth, symmetric reductions in cross-section with pronounced shear-lip formation. No premature cracking, interface separation, or delamination is observed at either the inner or outer surface. Higher-magnification digital microscope images of specimen 4 confirm that the fracture surface displays a rough, fibrous appearance with equiaxed dimples and no planar facets or cleavage-like features.

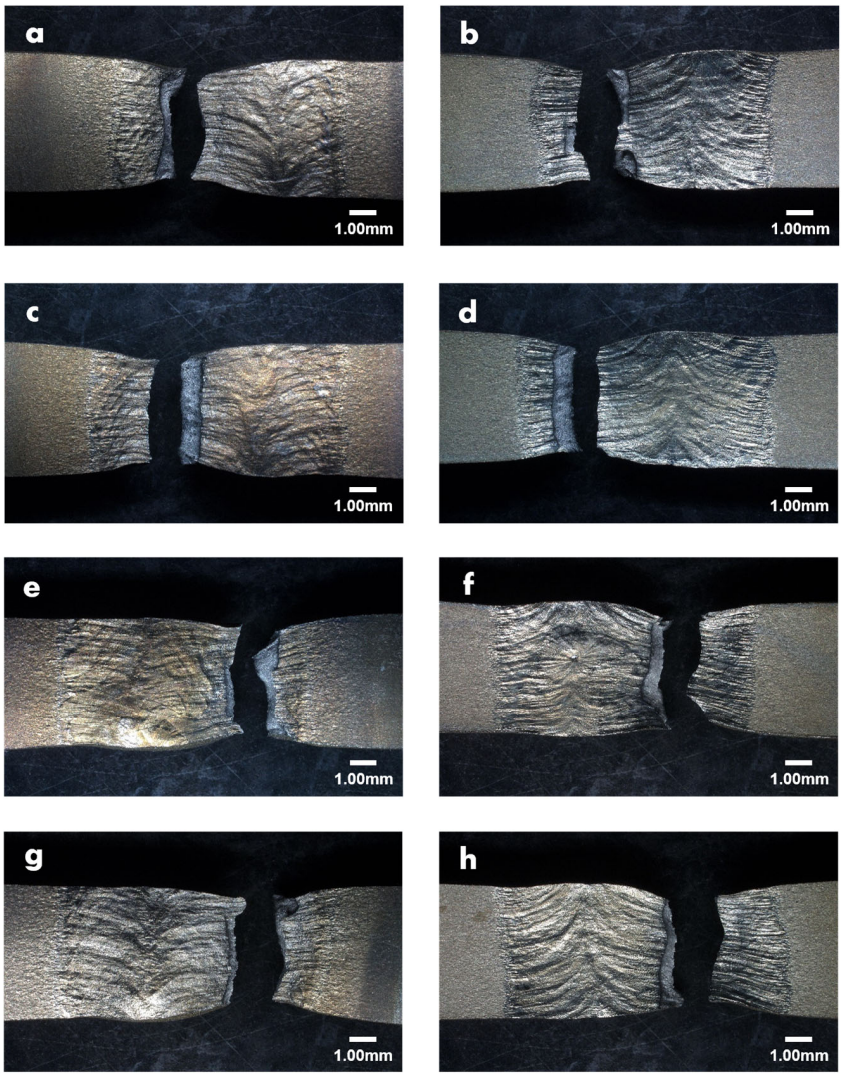

Figure 5. Macroscopic appearance of four cross-weld tensile specimens after fracture: (**a**,**b**) Specimen 1; (**c**,**d**) Specimen 2; (**e**,**f**) Specimen 3; (**g**,**h**) Specimen 4—each shown from front and back. All specimens show necking and shear-lip formation near the orbital GTAW weld. Scale bars: 1.00 mm.

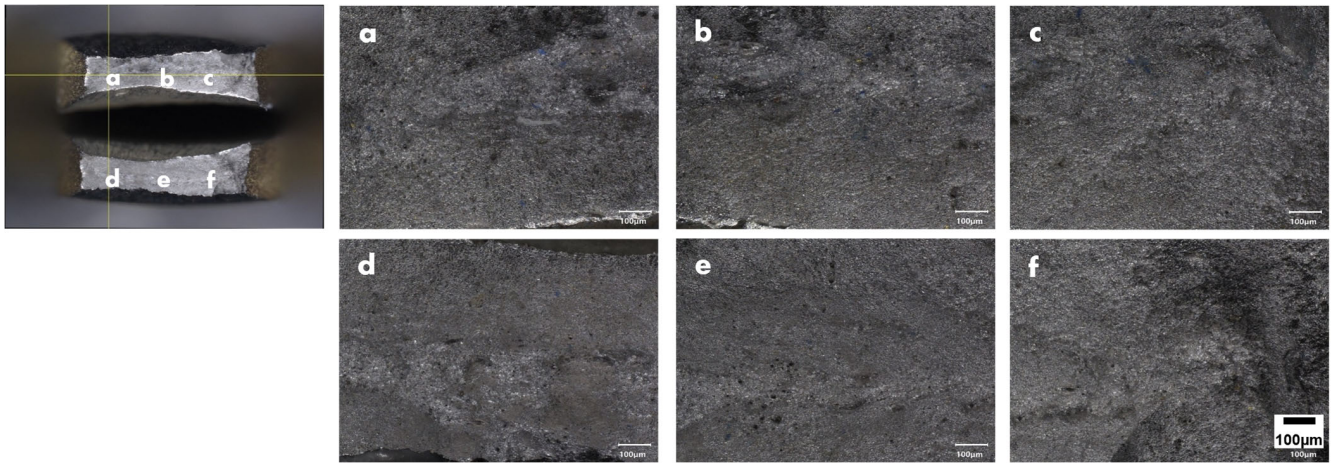

Figure 6. Digital microscope fractographs of Specimen 4: macroscopic overview (**left**) with observation positions (**a**–**f**) on the two mating fracture surfaces. (**a**–**c**) One fracture surface; (**d**–**f**) the opposite fracture surface. All regions exhibit fibrous fracture morphology with equiaxed dimples and no cleavage features, confirming fully ductile failure. Scale bars: 100 µm (all images).

Representative SEM fractographs taken from cross-weld tensile Specimen 1 are shown in Figure 7. The images were acquired at ×1000 magnification from sequential through-thickness positions on the two opposing fracture surfaces. On one side of the fracture surface (Figure 7a,c,e,g), the morphology evolves from the outer surface through the upper mid-thickness and lower mid-thickness to the inner surface, while the corresponding positions on the opposite side (Figure 7b,d,f,h) reveal the same characteristic features from the complementary perspective. All regions exhibit a homogeneous dimpled morphology associated with microvoid nucleation, growth, and coalescence, confirming a fully ductile fracture mode. No cleavage facets, intergranular decohesion features, or defect-related fracture origins were observed at any through-thickness location, indicating that the circumferential orbital GTAW weld did not introduce brittle regions or critical defects that would localize fracture.

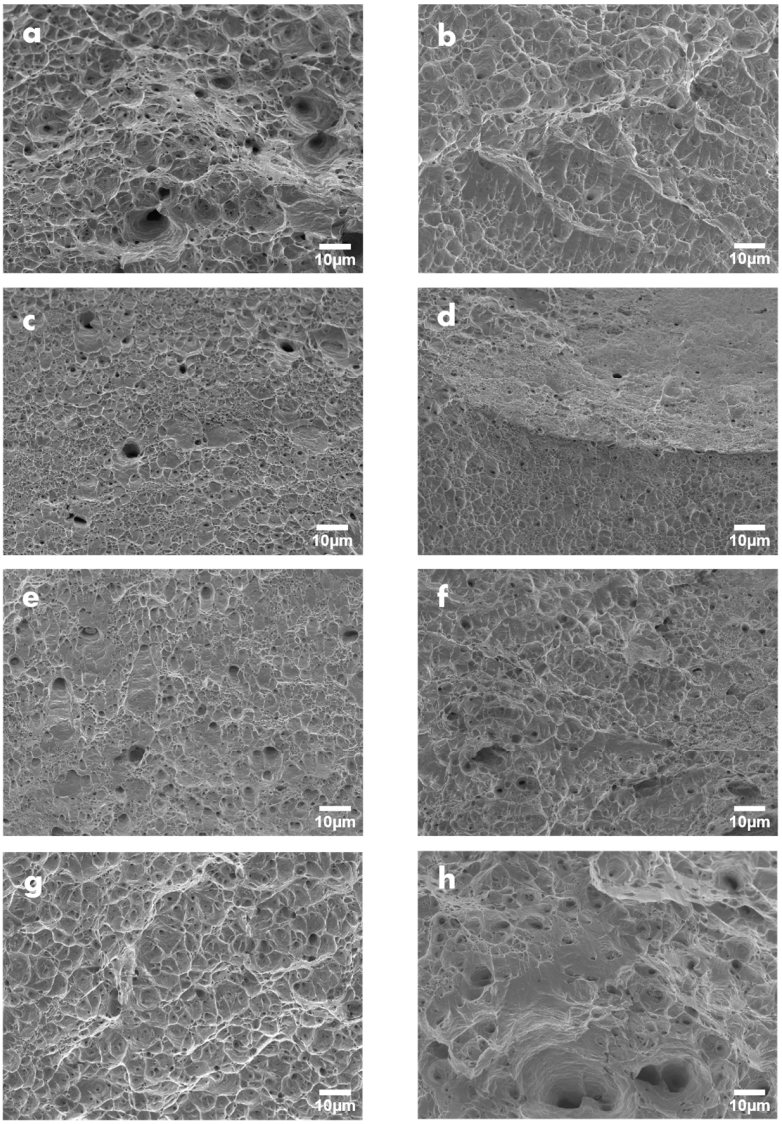

Figure 7. SEM fractographs of cross-weld tensile Specimen 1 at ×1000 magnification taken from sequential through-thickness positions on the two opposing fracture surfaces. (**a**,**c**,**e**,**g**) Views from one side of the fracture surface, from the outer surface through the upper mid-thickness and lower mid-thickness to the inner surface. (**b**,**d**,**f**,**h**) Corresponding positions on the opposite fracture surface, including the mid-thickness transition zone (**d**) and the shear-lip region near the outer surface (**h**). All regions exhibit a ductile dimpled morphology characteristic of microvoid coalescence, with no evidence of cleavage or intergranular decohesion.

4. Discussion

4.1. Microstructural Evolution in the Longitudinal Seam and Orbital GTAW Welds

The EBSD results demonstrate that the longitudinal seam weld and the circumferential orbital GTAW welds exhibit distinct but related austenitic microstructures that reflect both the prior thermo-mechanical processing of the pipe and the subsequent welding thermal cycles. In the longitudinal seam weld, the fusion zone is dominated by epitaxially grown columnar γ-austenite grains extending from the fusion boundaries toward the weld centerline, while the adjacent base metal (BM) retains a rolled austenitic microstructure containing elongated grains and δ-ferrite stringers aligned along the pipe axis. The heat-affected zone (HAZ) is relatively narrow and consists of equiaxed grains with an increased population of Σ3 twin boundaries, indicating that partial recrystallization occurred during seam welding and subsequent pipe forming [2,3,15]. For the circumferential orbital GTAW welds, EBSD grain size analysis reveals that the average equivalent circle diameter in the weld metal (WM) is in the order of 45 ± 15 μm, compared with approximately 28 ± 8 μm in the BM and 32 ± 10 μm in the HAZ. Thus, the WM grains are roughly 60% larger than those of the BM, whereas the HAZ exhibits an intermediate grain size, reflecting limited grain growth during the orbital welding thermal cycle rather than extensive coarsening. In each region, more than 500 grains were analyzed, ensuring statistical robustness of the grain size measurements.

The grain boundary character distribution further quantifies the effect of the thermal cycles. The fraction of high-angle grain boundaries (HAGBs, $\theta \geq 15^\circ$) in the WM, HAZ, and BM is approximately 78–80%, 72–73%, and 76–77% of the total boundary length, respectively, while the corresponding low-angle grain boundary (LAGB, $2^\circ \leq \theta < 15^\circ$) fractions are about 20–22%, 27–28%, and 23–24%. The elevated LAGB fraction in the HAZ relative to both the WM and BM suggests that deformation subgrains are retained, which is characteristic of incomplete recrystallization. The Σ3 twin boundary length fraction increases from about 8% in the WM to roughly 16% in the HAZ and 12% in the BM, corresponding to an approximately two-fold (≈91%) increase between the WM and HAZ. This marked increase in Σ3 content provides quantitative evidence for annealing-twin formation during grain boundary migration in the partially recrystallized HAZ.

Kernel average misorientation (KAM) maps complement these observations by highlighting the distribution of local lattice curvature and geometrically necessary dislocation (GND) density. The average KAM values in the WM, HAZ, and BM are in the order of 1.5–2.0°, 1.0–1.3°, and 0.7–1.0°, respectively, when calculated with a 5° misorientation threshold. The higher KAM levels in the WM and in the vicinity of the fusion boundaries reflect the high thermal gradients and solidification stresses associated with autogenous GTAW, whereas the reduction in KAM in the HAZ is consistent with recovery and partial recrystallization relieving stored deformation energy. The BM, away from the welds, exhibits the lowest average KAM values, although locally elevated KAM is observed around δ-ferrite stringers introduced during pipe rolling. Similarly, the measured HAGB/LAGB balance and KAM distributions in the weld metal, HAZ, and base metal follow trends reported in recent work where grain boundary character distribution and local misorientation were used to track recovery and recrystallization stages in welded microstructures [10,20,23–27].

4.2. Metallurgical Significance of the Three-Segment Orbital GTAW Procedure

The three-segment orbital GTAW procedure employed in this work was designed to balance full penetration, microstructural homogenization, and crack-free weld termination in thin-walled (t = 2.0 mm) 304 stainless steel seam pipes. Based on the nominal arc efficiency ($\eta \approx 0.7$), arc voltage ($V \approx 12$ V), measured currents, and travel speeds, the

calculated heat inputs for the first, second, and third segments are approximately 0.10, 0.09, and 0.09 kJ/mm, respectively.

The first segment, operated at the highest peak current for a duration of roughly 30 s, establishes the initial weld pool and achieves through-thickness penetration without burn-through, thereby avoiding lack-of-fusion defects that are common in single-pass autogenous welding of thin sections. The second segment, with a slightly reduced peak current and a longer duration of about 60 s, acts as a remelting and homogenization stage: a substantial portion of the first-segment weld metal is partially remelted, promoting redistribution of δ-ferrite stringers, healing of incipient porosity or micro-cracks through liquid-phase mechanisms, and smoothing of solidification structures. This repeated thermal cycling contributes to a more uniform columnar grain morphology and reduces the likelihood of centerline defects.

The third segment corresponds to a short downslope (crater-fill) stage, lasting approximately 1.7 s, during which the current is gradually reduced rather than abruptly terminated. Although it does not constitute a full additional pass, this segment plays a crucial metallurgical role by filling the end crater and minimizing geometric discontinuities and shrinkage stresses at the weld termination. The absence of crater cracking or other termination-related defects in the macro- and microstructural observations, together with the highly reproducible mechanical response of the tensile specimens, confirms that the three-segment procedure effectively controls both penetration and defect formation for the present pipe geometry [7,11,12,28].

4.3. Quantitative Microstructure–Property Relationships

The Vickers microhardness profiles across the longitudinal seam weld and the circumferential orbital GTAW welds show only modest variations and no evidence of severe HAZ softening or excessive hardening. In the longitudinal seam weld, the average hardness values in the BM, HAZ, and WM are approximately 190–195 HV, 200–205 HV, and 205–210 HV, respectively, indicating that the WM is roughly 10–15 HV harder than the BM but remains relatively uniform across the fusion zone. In the orbital welds, the corresponding hardness levels are in the order of 195–205 HV (BM), 200–210 HV (HAZ), and 200–215 HV (WM). The hardness differences between WM and BM are generally within 10%, and the HAZ hardness consistently lies between these extremes, demonstrating the absence of a pronounced softened or over-hardened band.

From a Hall–Petch perspective, the coarser grain size in the WM relative to the BM would normally be expected to reduce strength and hardness, according to $\sigma_y = \sigma_0 + k_y d^{-\frac{1}{2}}$. However, the observed decrease in hardness relative to the BM is small, and in some cases the WM is slightly harder than the BM. This apparent deviation from a simple grain-size scaling can be rationalized by considering the higher dislocation density in the WM, as reflected by the elevated KAM values, and the presence of δ-ferrite, both of which contribute to strengthening and partially compensate for grain coarsening. Conversely, the HAZ, which exhibits an increased Σ3 twin boundary fraction and a higher LAGB fraction relative to the WM, displays hardness values only slightly below or comparable to those of the WM. The increased Σ3 content and reduced KAM in the HAZ indicate partial recrystallization and reduced stored energy, which tends to soften the material, but the effect remains moderate because the overall grain size is still relatively fine. The cross-weld tensile properties corroborate this microstructural picture. The four cross-weld specimens exhibit an average yield strength, ultimate tensile strength, and total elongation of approximately 205 ± 8 MPa, 665 ± 15 MPa, and 38 ± 2%, respectively, compared with 215 ± 5 MPa, 680 ± 10 MPa, and 42 ± 2% for the as-received base metal. Thus, the orbital GTAW welds retain roughly 95% of the base-metal strength and about 90% of the ductility.

The coefficients of variation for ultimate tensile strength and elongation are in the order of 2–3%, indicating highly reproducible mechanical behavior. Necking consistently localizes in the weld region, which is slightly softer than the work-hardened BM, but the high fracture strains and smooth engineering stress–strain curves confirm that the weldments preserve a favorable strength–ductility balance.

The observed hardness variations (in the order of 10–20 HV) are small relative to the absolute hardness level and confined to a limited region around the weld. As a result, the average strength over the gauge length remains close to that of the base metal, and the cross-weld tensile properties are not significantly degraded. In other words, the local hardness differences are not large enough to induce a pronounced reduction in global tensile strength or ductility [2,8,23].

Taken together, the EBSD, hardness, and tensile data establish a coherent microstructure–property relationship: (i) the coarser, high-KAM WM retains adequate strength through dislocation and δ-ferrite strengthening despite grain coarsening; (ii) the HAZ with elevated Σ3 and LAGB fractions exhibits partial recrystallization and moderate hardness; and (iii) the rolled BM possesses relatively fine grains and slightly higher strength but does not introduce brittle behavior. The result is a nearly uniform and mechanically robust cross section.

4.4. Fracture Behavior and Implications for Structural Integrity

FE-SEM fractography of a representative cross-weld specimen provides further insight into the failure mechanisms. Fractographs taken at eight through-thickness positions on the two opposing fracture surfaces show a consistently dimpled morphology characteristic of microvoid nucleation, growth, and coalescence. The dimples typically range from 1 to 5 μm in diameter, with occasional larger dimples containing secondary particles or small voids that acted as microvoid nucleation sites. The outer surface, upper and lower mid-thickness, and inner surface regions all exhibit similar dimple populations, and the corresponding locations on the opposite fracture surface display essentially identical features.

No cleavage facets, intergranular decohesion, or defect-controlled crack initiation sites are observed at any position, and there is no evidence of fracture originating from welding defects such as porosity, lack of fusion, or slag inclusions. This uniform ductile fracture mode is fully consistent with the high elongations and smooth stress–strain curves, as well as with the absence of severely embrittled layers or extreme hardness gradients in the weldments. Although Figure 7 illustrates only a single specimen, the remaining cross-weld specimens exhibit similar dimpled fracture morphologies, confirming the reproducibility of the fully ductile failure mode [3,6,16].

From a structural integrity standpoint, these observations indicate that the three-segment autogenous orbital GTAW procedure employed here produces joints that are free of critical metallurgical weaknesses and suitable for high-purity piping applications where leak-tightness and mechanical reliability are essential. Further work comparing one-, two-, and three-segment procedures and integrating the present EBSD–hardness–tensile framework with non-destructive evaluation or thermophysical measurements could enable predictive, physics-based qualification of orbital welds in service. These observations suggest that the present EBSD-derived descriptors (grain size, Σ3 fraction, HAGB/LAGB ratio, KAM distributions) could be incorporated into emerging predictive microstructure–property frameworks that link crystallographic texture and grain boundary statistics to elastic response and strength, as demonstrated in recent texture–property correlation studies [28–31].

In addition, no non-metallic inclusions or inclusion-induced fracture origins were detected on any of the observed fracture surfaces, indicating that the orbital GTAW process did not introduce inclusion-related defects and is therefore compatible with the stringent particle-cleanliness requirements of semiconductor process piping.

5. Conclusions

1. EBSD analysis revealed that the weld metal in both the longitudinal seam and circumferential orbital GTAW joints consists of epitaxially grown columnar austenite grains with strong preferred orientations aligned with the solidification direction, whereas the HAZ exhibits finer equiaxed grains with a significantly increased Σ3 twin boundary fraction and elevated LAGB content. These features provide direct evidence of partial recrystallization induced by the welding thermal cycles, while the HAZ remains narrow and indistinct owing to the rapid cooling and the inherent stability of the austenitic matrix.
2. IPF-BCC mapping confirmed that δ-ferrite is present only as sparse, discontinuous stringers within the fusion zone and along the rolled base metal, with no continuous δ network or massive secondary phases detected. KAM maps quantified the distribution of the local lattice curvature and showed relatively low average misorientation in the central weld metal but increased KAM along the fusion boundaries and in regions affected by prior pipe forming, reflecting the combined effects of thermal mismatch and residual cold-work strain.
3. Vickers microhardness profiles across the longitudinal seam weld and the two circumferential orbital GTAW welds showed only modest variations between the weld metal, HAZ, and base metal, with hardness differences typically within about 10–20 HV and no pronounced HAZ softening or excessive hardening. The seam weld metal exhibited the highest and most uniform hardness, whereas the orbital weld metals displayed slightly lower and more spatially variable hardness with mild through-thickness gradients characteristic of single-sided heat input, yet without creating critically weakened regions.
4. Cross-weld tensile tests performed in accordance with ASTM E8/E8M-22 demonstrated yield strengths above 200 MPa, ultimate tensile strengths in the order of 650–680 MPa, and total elongations approaching 40%, indicating that the autogenous orbital GTAW weldments retain mechanical properties comparable to those of the as-received seam pipe. The scatter in tensile properties among four cross-weld specimens was small, confirming the reproducibility of the three-segment orbital procedure.
5. SEM fractography from multiple through-thickness positions on the two opposing fracture surfaces of the cross-weld specimens showed a uniformly dimpled morphology associated with microvoid nucleation, growth, and coalescence, with no evidence of cleavage facets, intergranular decohesion, or fracture initiated at weld defects such as porosity or lack of fusion. Furthermore, no non-metallic inclusions were observed on the fracture surfaces, suggesting that the orbital GTAW procedure does not introduce inclusion-related defects and is suitable for semiconductor manufacturing lines where particle cleanliness is critical.

Overall, the integrated EBSD–hardness–tensile–fractography results demonstrate that the three-segment autogenous circumferential orbital GTAW procedure produces structurally sound, fully ductile joints in commercially rolled 304 stainless steel seam pipes while preserving strength and ductility close to those of the base material. This provides a microstructurally informed and quantitatively supported basis for qualifying and further optimizing orbital welding procedures for high-purity industrial fluid distribution systems. In future work, the tensile and fracture properties of salt-spray-exposed weldments will be investigated to assess the influence of corrosive environments on the long-term mechanical integrity of these orbital GTAW joints.

Supplementary Materials: The following supporting information can be downloaded at: https://www.mdpi.com/article/10.3390/met16060565/s1.

Author Contributions: Conceptualization, B.J.; methodology, B.J.; validation, B.J.; resources, B.J.; software, E.P.; data curation, E.P.; writing—original draft preparation, E.P.; writing—review and editing, B.J.; supervision, B.J.; project administration, B.J. All authors have read and agreed to the published version of the manuscript.

Funding: This research received no external funding.

Data Availability Statement: The original contributions presented in this study are included in the article/Supplementary Materials. Further inquiries can be directed to the corresponding author.

Conflicts of Interest: The authors declare no conflict of interest.

References

1. Niagaj, J.; Jędrusiak, A. The Effect of Shielding Gas Composition and Orbital TIG Welding Parameters on the Dimensions and Quality of Austenitic Stainless Steel Pipe Girth Welds. *Research* **2015**, *1*, 5–12.
2. Widyianto, A.; Baskoro, A.S.; Kiswanto, G. Investigation on Weld Characteristic, Welding Position, Microstructure, and Mechanical Properties in Orbital Pulse Current Gas Tungsten Arc Welding of AISI 304L Stainless Steel Pipe. *Int. J. Technol.* **2022**, *13*, 473–483. [CrossRef]
3. Dak, G.; Pandey, C. Microstructure Anomaly during Welding and Its Influence on the Mechanical Properties of Dissimilar Weldments of P92 Martensitic Steel and AISI 304L Austenitic Stainless Steel. *J. Manuf. Process.* **2022**, *80*, 829–852. [CrossRef]
4. Lee, S.-J.; Lai, J.-J. The Effects of Electropolishing (EP) Process Parameters on Corrosion Resistance of 316L Stainless Steel. *J. Mater. Process. Technol.* **2003**, *140*, 206–210. [CrossRef]
5. Mousavi, B.; Shakeri, M.S.; Shamsipoor, A. Slurry Erosion Characteristics of Stellite 6 on AISI 316 and AISI 410 Stainless Steels. *J. Weld. Join.* **2020**, *38*, 584–592. [CrossRef]
6. Tabrizi, T.R.; Sabzi, M.; Mousavi Anijdan, S.H.; Eivai, A.R.; Park, N.; Jafarian, H.R. Comparative Study of Orbital Welding and Manual Welding for 316L Stainless Steel Tube Joints. *J. Mater. Res. Technol.* **2021**, *15*, 199–212. [CrossRef]
7. Alves, A.R.; Costa, J.F.; Santos, R.G. The Effect of Repeated Welding Cycles on the Microstructure and Ferrite Content of 25Cr Super Duplex Stainless Steel Weld Metal by Automatic Orbital TIG Welding. *ARPN J. Eng. Appl. Sci.* **2016**, *11*, 11982–11987.
8. Pham, S.M.; Nguyen, V.-T.; Do, T.T.; Uyen, T.M.T.; Toan, H.D.S.; Linh, H.T.T.; Nguyen, V.T. Parameter Optimization in Orbital TIG Welding of SUS 304 Stainless Steel Pipe. *Metals* **2024**, *14*, 5. [CrossRef]
9. Saravanan, S.; Sivagurumanikandan, N.; Raghukandan, K. Effect of Heat Input on Microstructure and Mechanical Properties of Nd:YAG Laser Welded Super Duplex Stainless Steel—Numerical and Experimental Approach. *Int. J. Press. Vessel. Pip.* **2019**, *185*, 447–455.
10. Deng, D.; Murakawa, H. Numerical Simulation of Temperature Field and Residual Stress in Multi-Pass Welds in Stainless Steel Pipe and Comparison with Experimental Measurements. *Comput. Mater. Sci.* **2006**, *37*, 269–277. [CrossRef]
11. Riffel, K.C.; Silva, R.H.G.; Dalpiaz, G.; Marques, C.; Schwedersky, M.B. Comparing the Effect of Continuous and Pulsed Current in the GTAW Process of AISI 316L Stainless Steel Welded Joint: Microstructural Evolution, Phase Equilibrium, Mechanical Properties and Fracture Mode. *J. Mater. Res. Technol.* **2021**, *15*, 199–212. [CrossRef]
12. Riffel, K.C.; Silva, R.H.G.; Dalpiaz, G.; Marques, C.; Schwedersky, M.B. Keyhole GTAW with Dynamic Wire Feeding Applied to Orbital Welding of 304L SS Pipes. *Soldag. Inspeção* **2019**, *24*, e2418. [CrossRef]
13. Fadaei, M.R.; Poursina, A.M.A. Thermal Aging Effect on Fracture Toughness of GTAW/SMAW of 316L Stainless Steel: Experiments and Applicability of Existing CASS Models. *Nucl. Eng. Technol.* **2021**, *53*, 1357–1368. [CrossRef]
14. Park, D.; Song, C.; Park, Y. A Study on Gap Bridging Formation Conditions in Butt Root Pass Welding Using GTAW. *J. Weld. Join.* **2023**, *41*, 335–341. [CrossRef]
15. Chen, C.; Li, W.; Sun, X.; Feng, T.; Du, W.; Zhao, X. Ultrasonic-Magnetic Field Coaxial Hybrid Controlling the Microstructure and Mechanical Properties of 304 Stainless Steel GTAW Joints. *J. Mater. Res. Technol.* **2023**, *25*, 5807–5819. [CrossRef]
16. Hosseinzadeh, F.; Tafazzoli-Moghaddam, B.; Kim, H.K.; Bouchard, P.J.; Akrivos, V.; Vasileiou, A.N.; Smith, M. Residual Stresses in Austenitic Thin-Walled Pipe Girth Welds: Manufacture and Measurements. *Int. J. Press. Vessel. Pip.* **2023**, *206*, 105016. [CrossRef]
17. Jafarzadegan, M.; Taghiabadi, R.; Mofid, M.A. Using Double Ellipsoid Heat Source Model for Prediction of HAZ Grain Growth in GTAW of Stainless Steel 304. *Mater. Today Commun.* **2022**, *31*, 103411. [CrossRef]
18. Wang, Y.; Wang, L.; Di, X.; Shi, Y.; Bao, X.; Gao, X. Simulation and Analysis of Temperature Field for In-Service Multi-Pass Welding of a Sleeve Fillet Weld. *Comput. Mater. Sci.* **2013**, *68*, 198–205. [CrossRef]
19. Zubairuddin, M.; Albert, S.K.; Vasudevan, M.; Mahadevan, S.; Chaudhari, V.; Suri, V.K. Numerical Simulation of Multi-Pass GTA Welding of Grade 91 Steel. *J. Manuf. Process.* **2017**, *27*, 87–97. [CrossRef]
20. Purmohamad, H.; Kermanpur, A.; Shamanian, M. Numerical Simulation and Experimental Investigation of Temperature Distribution in the Circumferentially Butt GTAW of Incoloy 800H Pipes. *Int. J. Press. Vessel. Pip.* **2010**, *87*, 424–432. [CrossRef]

21. *ASTM E8/E8M-22*; Standard Test Methods for Tension Testing of Metallic Materials. ASTM International: West Conshohocken, PA, USA, 2022.
22. *ASTM A312/A312M-13a*; Standard Specification for Seamless, Welded, and Heavily Cold Worked Austenitic Stainless Steel Pipes. ASTM International: West Conshohocken, PA, USA, 2013.
23. Mortazavi, E.; Najafabadi, R.A.; Meysami, A. Effect of Heat Input on Microstructure and Mechanical Properties of Dissimilar Joints of AISI 316L Steel and API X70 High-Strength Low-Alloy Steel. *J. Iron Steel Res. Int.* **2017**, *24*, 1248–1253. [CrossRef]
24. Hedaiat, F.; Dehmolaei, R.; Khorasanian, M.; Lotfi, B. Long-Term Oxidation Behaviour and Thermal Stability of Heat-Resistant Stainless Steel Claddings Deposited on AISI 316 Stainless Steel by the GTAW Process. *Surf. Coat. Technol.* **2021**, *424*, 127605. [CrossRef]
25. Garlea, E.; Choo, H.; Sluss, C.C.; Koehler, M.R.; Bridges, R.L.; Xiao, X.; Ren, Y.; Jared, B.H. Variation of elastic mechanical properties with texture, porosity, and defect characteristics in laser powder bed fusion 316L stainless steel. *Mater. Sci. Eng. A* **2019**, *763*, 138032. [CrossRef]
26. Tongjiao, C.; Wenjing, X.; Minghan, B. Insights into the Influence of Tensile and Compressive Strain on the Microstructure and Corrosion Performance of 304 L stainless Steel. *Metals* **2024**, *14*, 1281. [CrossRef]
27. Zeuner, A.T.; Ewenz, L.; Kalich, J.; Schöne, S.; Füssel, U.; Zimmermann, M. The Influence of Heat Treatment on the Microstructure, Surface Roughness and Shear Tensile Strength of AISI 304 Clinch Joints. *Metals* **2022**, *12*, 1514. [CrossRef]
28. Li, L.; Du, Z.; Sheng, X.; Zhao, M.; Song, L.; Han, B.; Li, X. Comparative Analysis of GTAW+SMAW and GTAW Welded Joints of Duplex Stainless Steel 2205 Pipe. *Int. J. Press. Vessel. Pip.* **2022**, *199*, 104748. [CrossRef]
29. Fan, K.; Liu, B.; He, B.; Luo, Z. High-density low-angle grain boundaries enable exceptional combination of strength, ductility and toughness in 304 stainless steel. *J. Mater. Sci. Technol.* **2025**, *238*, 191–198. [CrossRef]
30. Hou, J.; Chen, W.; Chen, Z.; Zhang, K.; Huang, A. Microstructure, tensile properties and mechanical anisotropy of selective laser melted 304L stainless steel. *J. Mater. Sci. Technol.* **2020**, *48*, 63–71. [CrossRef]
31. Ghosh, N.; Roy, A. Taguchi Optimization of Microstructure and Mechanical Properties in Dissimilar TIG Welding of AISI 304 L–409 M Stainless Steel. *Sci. Rep.* 2026; *in press*. [CrossRef]